Transformations of Ferrihydrite-Extracellular Polymeric Substance Coprecipitates Driven by Dissolved Sulfide : Interrelated Effects of Carbon and Sulfur Loadings

Wang, Qihuang; Wang, Jiajia; Wang, Xingxing; Kumar, Naresh; Pan, Zezhen et al

Transformations of Ferrihydrite−Extracellular Polymeric Substance Coprecipitates Driven by Dissolved Sulfide: Interrelated Effects of Carbon and Sulfur Loadings

Qihuang Wang, Jiajia Wang,* Xingxing Wang, Naresh Kumar, Zezhen Pan, Stefan Peiffer, and Zimeng Wang*

Read Online

ACCESS | Metrics & More | Article Recommendations | Supporting Information

ABSTRACT: The association of poorly crystalline iron (hydr)-oxides with organic matter (OM), such as extracellular polymeric substances (EPS), exerts a profound effect on Fe and C cycles in soils and sediments, and their behaviors under sulfate-reducing conditions involve complicated mineralogical transformations. However, how different loadings and types of EPS and water chemistry conditions affect the sulfidation still lacks quantitative and systematic investigation. We here synthesized a set of ferrihydrite−organic matter (Fh−OM) coprecipitates with various model compounds for plant and microbial exopolysaccharides (polygalacturonic acids, alginic acid, and xanthan gum) and bacteriogenic EPS (extracted from *Bacillus subtilis*). Combining wet chemical analysis, X-ray diffraction, and X-ray absorption spectroscopic techniques, we systematically studied the impacts of C and S loadings by tracing the temporal evolution of Fe mineralogy and speciation in aqueous and solid phases. Our results showed that the effect of added OM on sulfidation of Fh−OM coprecipitates is interrelated with the amount of loaded sulfide. Under low sulfide loadings (S(-II)/Fe < 0.5), transformation to goethite and lepidocrocite was the main pathway of ferrihydrite sulfidation, which occurs more strongly at pH 6 compared to that at pH 7.5, and it was promoted and inhibited at low and high C/Fe ratios, respectively. While under high sulfide loadings (S(-II)/Fe > 0.5), the formation of secondary Fe−S minerals such as mackinawite and pyrite dominated ferrihydrite sulfidation, and it was inhibited with increasing C/Fe ratios. Furthermore, all three synthetic EPS proxies unanimously inhibited mineral transformation, while the microbiogenic EPS has a more potent inhibitory effect than synthetic EPS proxies compared at equivalent C/Fe loadings. Collectively, our results suggest that the quantity and chemical characteristics of the associated OM have a strong and nonlinear influence on the extent and pathways of mineralogical transformations of Fh−OM sulfidation.

KEYWORDS: iron mineral transformation, iron mineral sulfidation, organic matter−mineral interactions, dissolved organic matter, extracellular polymeric substances
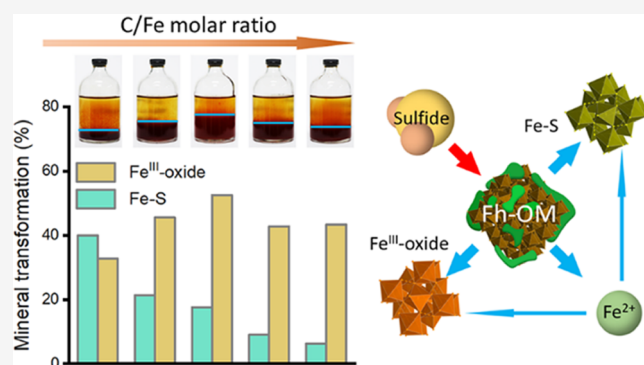
INTRODUCTION

The interaction between poorly crystalline Fe(III)-(hydr)-oxides, such as ferrihydrite (Fh), and dissolved sulfide is a prominent pathway of electron transfer in many anoxic environments, such as in flooded soils and oceans or lake sediments.[1−3] Sulfide-induced ferrihydrite mineralogical transformations include the formation of Fe−S secondary minerals, such as mackinawite and finally pyrite,[1,4] and Fe(II)-catalyzed recrystallization of Fe(III)-oxides (e.g., lepidocrocite, goethite, and magnetite). Ferrihydrite sulfidation may alter its chemical reactivity and surface morphology,[5,6] potentially affecting mineralogical stability, bioavailability, and mobility of nutrients[7,8] and the geochemical behavior of many contaminants, such as arsenic, antimony, and uranium.[9−14]

Previous studies on the kinetics and pathways of ferrihydrite sulfidation have largely focused on pure Fe minerals.[2,4,15−17] Fe(III)-(hydro)oxide sulfidation occurs over a wide pH interval and is considered to initiate pyrite formation and sulfur recycling.[2] This process is highly pH-dependent and reaches maximum reaction rates between pH 5.5 and 6.[11,18,19] Electron transfer between Fe(III)-(hydro)oxides and surface-complexed sulfide results in the reduction of Fe(III) and the

formation of S^0,[17] as well as the formation of metastable Fe–S phase.[1,17] Moreover, pyrite could be formed via the direct precipitation of excess Fe(II) and polysulfides, or reaction between metastable Fe–S species and dissolved polysulfides.[1,20] Kinetics and pathways of Fe(III)-(hydro)oxides pyritization are closely related to the S(-II)/Fe molar ratio.[1,2,16] Peiffer et al. demonstrated that the extent of secondary Fe minerals and pyrite formation is controlled by the capability of the Fe(III)-(hydro)oxides to conduct electrons from surface-associated Fe(II) to solid Fe(III) phase and the ratio between added sulfide and available surface area.[1] Wan et al. proposed a new ferric-hydroxide-surface pathway based on the formation of the precursor species $>Fe^{II}S_2^-$, which is competitive to $Fe-S_x$ precipitation at high DS(-II) concentrations for the rapid formation of pyrite. Hence, the pyrite formation rate decreases with the increase of the S(-II)/Fe molar ratio.[2] In addition, the reaction of Fe(III)-(hydro)oxides with DS(-II) also leads to the reductive iron dissolution, which rate is highly pH-dependent,[17,18,21] and the generated Fe(II) may potentially catalyze the transformation of ferrihydrite to crystalline Fe(III)-oxides.[22,23]

In natural soils and aquatic environments, ferrihydrite rarely exists as pure Fe phases but frequently associates with organic matter (OM) as mineral–organic coprecipitates under the influence of exudates from plants, algae, and bacteria.[24−26] Fh–OM coprecipitates, which have a wide range of C/Fe molar ratios up to 17.5,[27,28] play a vital role in the long-term preservation of organic C as well as influencing the properties and reactivity of Fh.[29,30] Compared with the pure Fh, Fh–OM coprecipitates have lower specific surface area owing to the blockage of mineral surface sites by OM and shows limited secondary mineral formation upon exposure to aqueous Fe(II).[31,32] Previous studies showed that adding OM with a range of molecular weights and carboxyl richness significantly suppresses sulfide-induced ferrihydrite transformations.[33−35] This could attribute to the strong binding of the carboxylic content on the mineral surface that reduces its reactivity. Moreover, the low-molecular-weight OM with high charge density may inhibit mineral aggregation and growth through Ostwald ripening.[36,37] Ferrihydrite sulfidation, in turn, could impact the fate of associated OM, such as its stability and molecular fractionation, in sulfidic conditions.[38−42]

Despite the known importance of Fh–OM coprecipitation in influencing Fh biogeochemical reactivity, sparse data exist about the influence of organic matter (OM) on sulfide-induced Fh transformations. A recent study of ThomasArrigo et al. showed that OM could influence transformation products of Fh exposed to sulfide, suggesting that Fh sulfidation pathways should include OM to better represent real environmental conditions.[33] However, how ferrihydrite sulfidation is affected by carbon loading over a wide range of C/Fe molar ratios remains elusive. Although limited, existing studies on the sulfidation of pure Fh[1,2,11] and influence of coprecipitated OM on Fe(II)-catalyzed Fh transformation[31,43] suggest that the anoxic reductive dissolution of ferrihydrite and its pyritization under OM loading depend on various factors, including OM properties, C/Fe ratio, S(-II)/Fe ratio, and pH.[1,11] Yet, few studies have systematically evaluated the impact of the abovementioned factors as well as their interactions on the sulfidation of Fh–OM coprecipitates. In porewaters of OM-rich wetland and estuarine sediments, both C/Fe molar ratios (0.2−25.0)[27,44] and DS(-II) concentrations (0.023−5.0 mM)[45−47] have wide spectrum. Considering the controlling

effect of the S(-II)/Fe molar ratio in pure Fh sulfidation,[1,2] we therefore hypothesize that the kinetics and mineralogical evolution pathways of Fh–OM sulfidation depend on the interrelated effects of carbon and sulfur loadings. Especially, the type and amount of secondary Fe phases such as crystalline Fe(III)-oxides and Fe–S minerals forming upon the reaction with DS(-II) are expected to differ between pure Fh and Fh–OM coprecipitates under a wide range of C/Fe ratio, S(-II)/Fe ratio, and pH.

In this study, we compared coprecipitations of ferrihydrite with different extracellular polymeric substance (EPS) proxies, including polysaccharides derived from plants, algae, and bacteria, as well as EPS extracted from *Bacillus subtilis*. EPS was selected because it constitutes an important fraction of the OM pool, and its coprecipitation with Fh has previously been shown to have a significant influence on the Fh properties such as specific surface area, porosity, and net charge.[48,49] Five C/Fe molar ratios, four S(-II)/Fe molar ratios, and two pH were set to reveal how EPS affects ferrihydrite sulfidation under broad water chemistry conditions. Accordingly, the objectives of this study were (1) to quantify the mineralogical transformation of DS(-II)-driven sulfidation of ferrihydrite−OM coprecipitations and (2) to evaluate the effect of the C/Fe molar ratio, S(-II)/Fe molar ratio, pH, and chemical composition of OM on mineralogical transformations under sulfidic conditions.

■ MATERIALS AND METHODS

Polysaccharides and Extracellular Polymeric Substances. Three macromolecular polysaccharides from different sources were selected as EPS proxies. Polygalacturonic acids $[(C_6H_8O_6)_n$, PGA] from plant species, alginic acid $[(C_6H_8O_6)_n$, AA] from brown algae, and xanthan gum $[(C_6H_8O_6)_n$, XG] of the bacterial strain *Xanthomonas campestris* were all purchased from Sigma-Aldrich.[50−52] Microbiogenic EPS was extracted from *B. subtilis* SBE1 (CCTCC AB 2018210). The *Bacillus* genus is the dominant soil aggregation bacteria with a high biofilm and EPS yield. EPS extracted from *B. subtilis* is commonly used as a representative EPS substance in biofilm and EPS research.[49,53−55] *B. subtilis* SBE1 was cultivated aerobically in LB-Lennox medium (5 g/L yeast extract, 10 g/L tryptone, 5 g/L NaCl) at 30 °C and 150 rpm on a horizontal shaker for 24 h to the early stationary growth phase. Bacterial cells in the suspension were removed by centrifugation (5000g, 15 min, 4 °C). The residual cells in decanted supernatant were removed by centrifugation (12,000g, 15 min, 4 °C). Cold reagent-grade ethanol at a ratio of 1:3 (v/v supernatant/ethanol) was added to the collected supernatant to precipitate crude EPS. After storage at 4 °C for 72 h, the precipitated crude EPS was separated from the mixture by centrifugation (12,000g, 15 min, 4 °C). To remove residual medium and ethanol for extraction, the crude EPS obtained by centrifugation was dialyzed against a cellulose membrane (Yuanye Biotechnology, 3500 MWCO) to get purified EPS. After 72 h of dialysis with Milli-Q water changes 3 times daily, the purified EPS solution was lyophilized and stored at 4 °C until use. The carbon content of EPS proxies and microbiogenic EPS was determined using a Vario EL cube CHNS analyzer (Table S1).

Ferrihydrite and Coprecipitate Synthesis. This experiment used deionized water (Milli-Q, Millipore, 18.2 MΩ·cm) to prepare all solutions. Following the previously reported procedures,[56] 2-line ferrihydrite and ferrihydrite−OM coprecipitation with initial C/Fe molar ratios of 0−3 in the solution

were synthesized. Pure ferrihydrite was synthesized by vigorously stirring (600 rpm) while adding 0.1 M NaOH to a 10 mM $Fe(NO_3)_3$ solution until a pH of 7 was reached. Ferrihydrite−OM coprecipitates were synthesized by dissolving 10 mM $Fe(NO_3)_3$ in an OM solution with different initial C/Fe molar ratios by adding 0.1 M NaOH under vigorous stirring (600 rpm) to pH 7. Both pure ferrihydrite and OM-ferrihydrite coprecipitates were washed and adjusted to pH 6.0 and pH 7.5 in 10 mM PIPES buffer. The PIPES buffer was chosen since it is a noncomplexing buffer that does not react with iron species.[57] Briefly, the synthetic ferrihydrite−OM coprecipitates containing PGA, AA, XG, and EPS extracted from *B. subtilis* are referred to as Fh-PGA, Fh-AA, Fh-XG, and Fh-EPS, respectively.

Sulfidation Experiments. The sulfidation experiments were conducted in triplicate in 50 mL of glass serum bottles wrapped in Al foil and performed in a glovebox system (Mikrouna, China) with a working atmosphere of N_2 (99.99%). Fh(−OM) slurry containing 10 mM Fe(III) with varied pH and C/Fe molar ratios was purged by pure N_2 for 30 min, transferred to 50 mL of glass serum bottles, and agitated for 24 h in the glovebox to eliminate residual oxygen while minimizing evaporation of the suspension. Three DS(-II) concentrations were set in this study to simulate the ferrihydrite sulfidation in different reducing environments (Figure S1). S(-II)/Fe molar ratios of 0.1, 0.5, and 1.0 are hereinafter referred to as low sulfide, medium sulfide, and high sulfide conditions, respectively. A certain amount of anoxic 100 mM $Na_2S \cdot 9H_2O$ stock solution was added to the ferrihydrite-(−OM) slurry with varied pH and C/Fe molar ratios according to the above S(-II)/Fe molar ratios. Iodometric titration was used to determine the concentration of sulfide stock solutions before addition. After adding sulfide, the suspensions in all serum bottles were quickly (less than 5 min) adjusted to the predetermined pH with 1 M HCl (Ultrapure, Adamas) to minimize H_2S gas evolution. Afterward, the serum bottles were crimped and sealed, wrapped with Al foil to prevent the sample from being affected by light, and set on an incubator shaker (180 rpm) at room temperature (25 ± 1 °C) until the sampling time. To avoid the effects of changes in headspace gas during sampling, serum bottles sampled at 1 day, 10 days, and 40 days were sacrificed, respectively. The experimental conditions of each serum bottle were summarized in Table S2. Photos of the suspension stand for different times after shaking were taken with a Canon M6 (50 mm, F1.8). All images were adjusted with consistent exposure and saturation parameters to ensure comparability among all treatment groups. The sulfidized suspension was rapidly transferred from the serum bottle to a centrifuge tube with a rubber seal in the glovebox and centrifuged (10,000g, 20 min) under anoxic conditions. The solid phase was washed with anoxic ultrapure water in the glovebox and centrifuged 3 times to remove impurities. All samples were lyophilized and stored in anoxic storage tanks until solid-phase characterization.

Wet Chemical Analysis. Iron and sulfur species in the aqueous phase during sample aging were determined by withdrawing 2 mL of the suspension from the serum bottles in the glovebox. The methylene blue method determined DS(-II) after filtration (0.22 μm, Nylon). However, this method can determine hydrogen sulfide, sulfide ions, and sulfide associated with aqueous polysulfide. Dissolved Fe(II) concentration was determined in 0.22 μm nylon filtrates photometrically with a Tecan photometer via the ferrozine method (λ = 570 nm).

The filtered liquid was mixed with hydroxylamine hydrochloride in a volume ratio of 1:4 and reacted for 30 min in the dark at room temperature, after which the total Fe concentration was determined as described above.

For determination of the total extractable iron, about 5 mg of the Fh−OM sample after centrifuging, washing, and freeze-drying was dissolved in 5 mL of 6 M HCl, heated at 60 °C for 3 days, and subsequently made up to a final volume of 50 mL with 1% HCl. HCl extractable Fe, which includes both amorphous Fe(III) and solid-phase-bound Fe(II), was extracted with 0.5 M HCl for 2 h and briefly purged with N_2.[1] The Fe(II) and total Fe were determined in the filtrate as previously mentioned. The 0.5 M HCl extractable Fe mainly contained the amorphous Fe phase like ferrihydrite,[58,59] while measured Fe(II) is primarily surface-adsorbed Fe(II). It is generally believed that in the difference between 6 M HCl and 0.5 M HCl extractable phases, Fe(III) is crystalline Fe(III)-oxides, such as goethite, magnetite, hematite, and lepidocrocite, while Fe(II) mainly contains sulfidized Fe(II) (i.e., the formation of Fe−S, except pyrite).[1]

Solid-Phase Characterization. The carbon content of Fh−OM samples before reaction with DS(-II) was determined using a Vario EL cube CHNS analyzer. Particle size distribution of nanoparticles was measured by multispectral advanced nanoparticle tracking analysis (MANTA) (ViewSizer 3000, MANTA Instruments Inc., San Diego, CA.) Microscopy images were obtained by scanning electron microscope (SEM) (Tescan Vega 3SBU, TESCAN Ltd., Brno, Czech Republic) equipped with a secondary electron (SE) detector operated at an acceleration voltage of 15 kV. Samples for X-ray diffractometry (XRD) analysis were mounted on the clean glass slides in the anoxic glovebox. To prevent oxidation, the slides were sealed with Kapton tape. Samples were scanned immediately after removal from the glovebox. All X-ray diffractograms were recorded with an X-ray diffractometer (Bruker D8-Advance) equipped with Cu Kα radiation generated at 40 kV and 40 mA. The XRD patterns were recorded from 10 to 80° 2θ with 0.05° of 2θ step-size and a 2 s acquisition time. Iron K-edge extended X-ray absorption fine structure (EXAFS) spectra of selected freeze-dried fine powder (200 mesh) solid-phase samples (Table S2) were conducted at Beamlines 20 of the Advanced Photon Source, Argonne National Laboratory. A Si double crystal monochromator was used with an energy resolution of 1.4×10^{-4} ($\Delta E/E$) at Fe K-edge. The incident beam was detuned 15% at 7.5 KeV. The scanning energy range for the Fe K-edge was set as 6960−7750 eV, with step sizes as 5 eV in the pre-edge region, 0.3 eV in X-ray absorption near-edge structure (XANES) region, and 0.05 Å^{-1} in the EXAFS region. The data collection time for each point was 1−2 s. The total acquisition time for each scan is 10−15 min. The detailed X-ray absorption spectroscopy (XAS) data analysis is presented in SI Text S1. Background subtraction and edge-height normalization were performed using the ATHENA program. Iron speciation was quantified using a series of reference standards and linear combination fitting (LCF) of the k^3-weighted EXAFS oscillations in the 1−11 Å^{-1} range. Ferrihydrite, goethite, mackinawite, hematite, pyrite, magnetite, and lepidocrocite were the initial reference standards for LCF. Only ferrihydrite, goethite, mackinawite, and lepidocrocite were included in the final LCF since other mineral phases comprised less than 10% of the LCF and were not found to improve the fit significantly. This spectrum selection is made following the corresponding XRD results. No
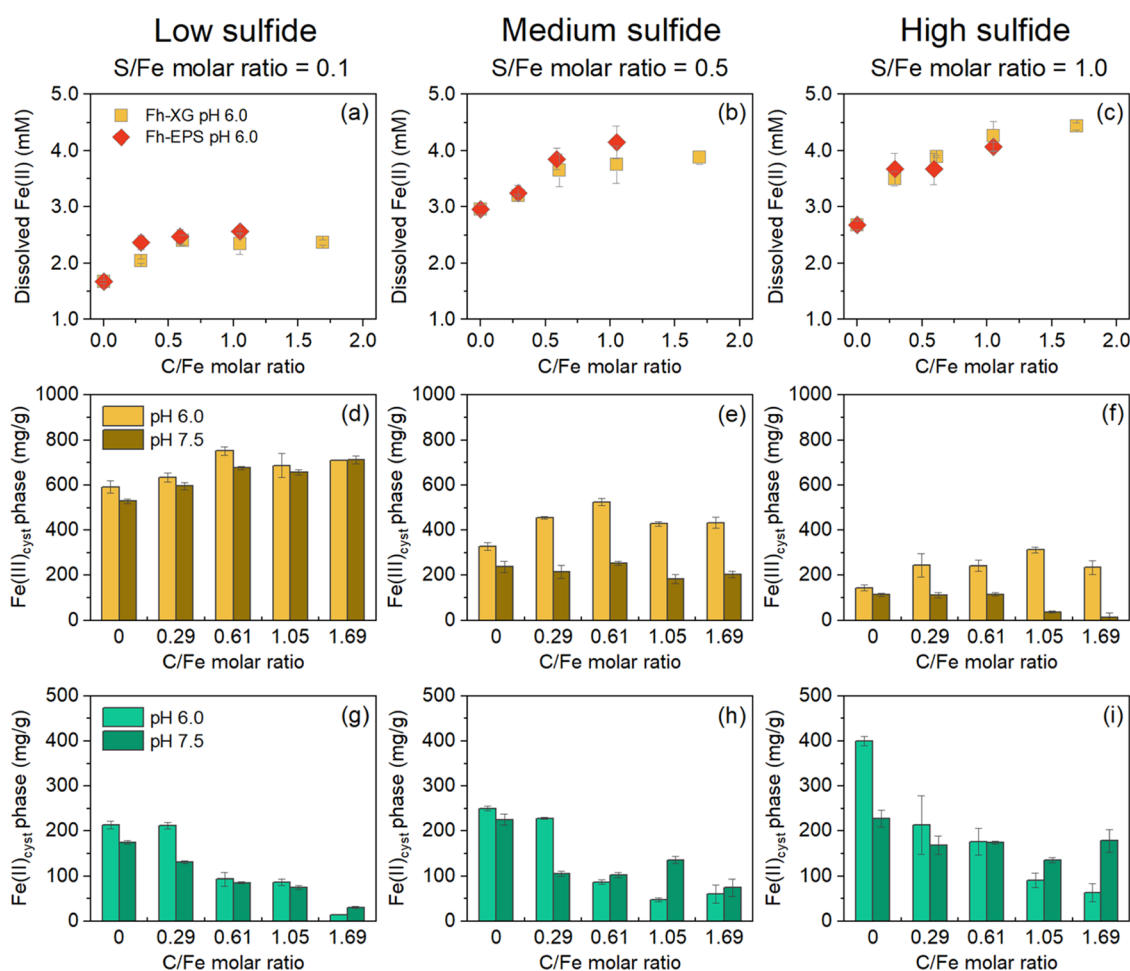
Figure 1. (a−c) Correlations of the equilibrium concentration of dissolved Fe(II) after Fh-XG coprecipitation (yellow) and Fh-EPS coprecipitation (red) reacted with S(−II) under low (a), medium (b), and high (c) sulfide conditions for 30 days at pH 6 with gradient C/Fe molar ratios. (d−i) The concentration of the crystalline Fe(II) phase (green) and crystalline Fe(III) phase (yellow) in the total solid iron phase after Fh-XG coprecipitation aging for 40 days at pH 6 (light) and pH 7.5 (dark) after the solid-phase fractions were treated by 0.5 M and 6 M HCl stepwise extraction.

energy shifts were permitted for fitting, and the sum of component species ranging between 0.72 and 1.03 was not constrained, but the results were normalized to 100%.

■ RESULTS

Macroscopy and Microscopy Images of Fh−OM Sulfidation. Adding different amounts of DS(-II) resulted in various color changes and particle precipitation of the Fh-XG coprecipitation. As shown in Figure S2, both pH 6 and 7.5 treatment groups under medium and high sulfide conditions turned black immediately. In contrast, the pH 6 and 7.5 treatment groups slowly turned dark brown and dark green under low sulfide conditions. The coprecipitation with 1, 10, and 40 day intervals was allowed to stand still for 24 h to ensure sufficient precipitation. The volume of the precipitation is positively correlated with the C/Fe molar ratio. After 24 h of reaction, the color change of all samples ceased substantially (Figure S2b). All of the treatment groups under medium and high sulfide conditions remained black after 40 days of sulfidation (Figure S2d). In the treatment group with the same C/Fe molar ratio, the volume of black particle flocs that were difficult to precipitate also increased with a higher S(-II)/Fe molar ratio. Pure ferrihydrite and Fh-XG coprecipitates showed varying surface morphologies by loading C and S

before and after sulfidation (Figures S3 and S4). The OM loading rendered the aged samples bulkier and more porous.

Total Aqueous Concentrations and Fe$_{aq}$ Speciation. Dissolved S(-II) concentrations decreased rapidly in all treatment groups, with 92−99% of the added DS(-II) consumed within 12 h, and fell to below the detection limit within 24 h at pH 7.5, except for the high sulfide treatment group, where DS(-II) was still detectable up to 48 h. In contrast, DS(-II) was consumed faster at pH 6, and almost no DS(-II) was detected within 12 h even in high sulfide treatments (Figures S5−S12g−i). The DS(-II) consumption rate in the high C/Fe molar ratio treatment groups was significantly slower than that of pure ferrihydrite. The concentrations of dissolved Fe(II) and total Fe in all treatment groups at pH 6 increased rapidly in the first 5 days, then decreased slowly, and finally plateaued (Figures S5−S12a−f). Dissolved Fe(II) constituted the majority of the total aqueous Fe. The subtle difference between Fe(II) and total Fe in the aqueous phase may be due to the organic complex Fe(III) formed by ferrihydrite and its secondary minerals during reductive dissolution and recrystallization. Dissolved Fe(II) concentrations after 30 days of equilibration in the Fh-XG and Fh-EPS systems positively correlate with the C/Fe molar ratio (Figure 1).
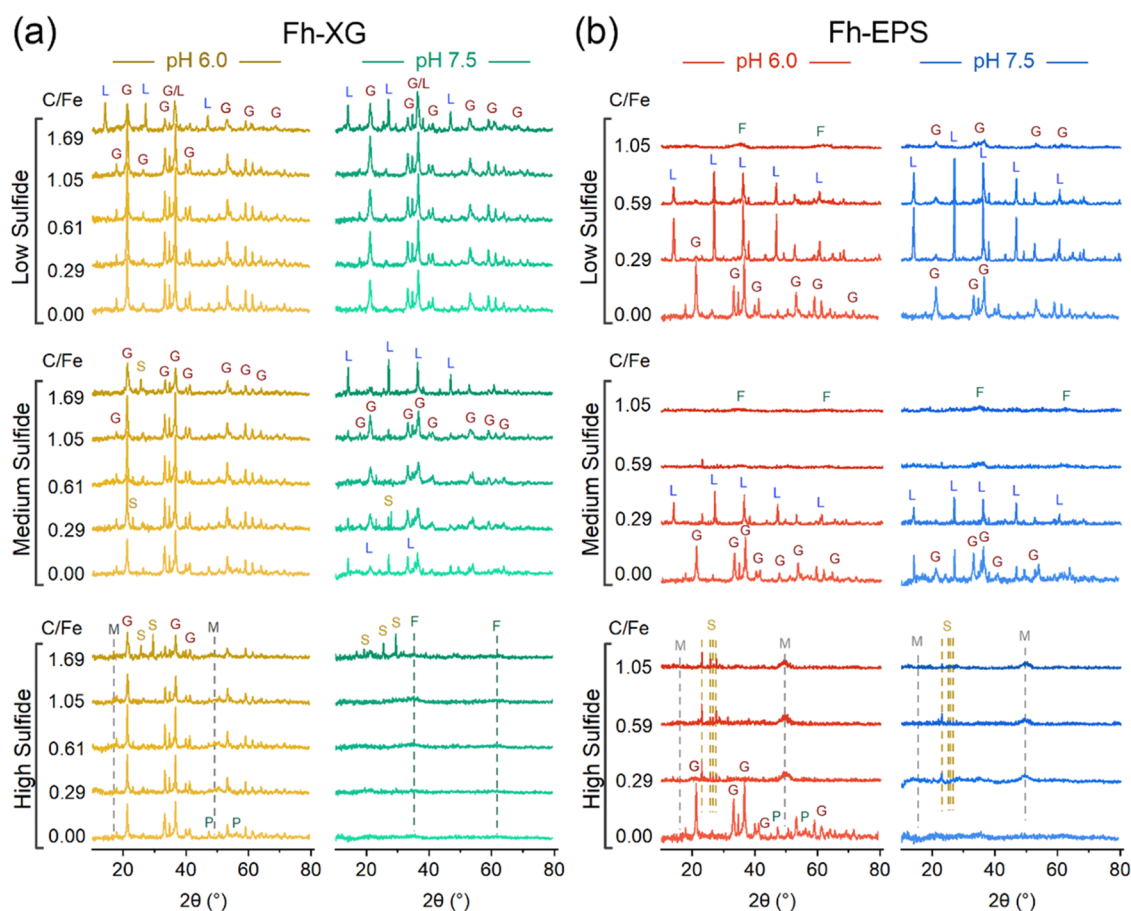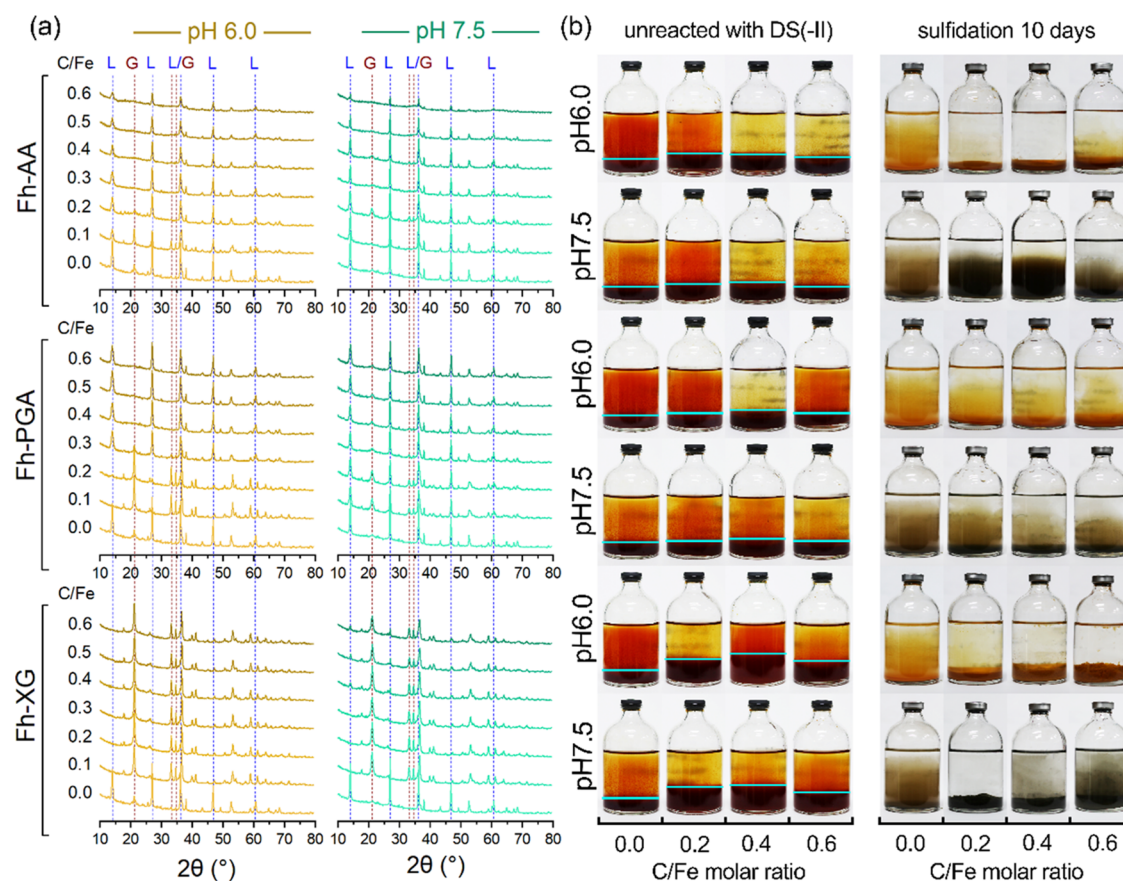
Figure 2. X-ray powder diffractograms of the Fh-XG (a) and Fh-EPS (b) coprecipitations after 40 days of aging following the addition of dissolved S(-II) at S(-II)/Fe molar ratios of 0.1, 0.5, and 1.0 at pH values 6 and 7.5. XRD pattern of the standard minerals used in the peak identification is shown in Figure S16. Abbreviations: G, goethite; L, lepidocrocite; M, mackinawite; P, pyrite; F, ferrihydrite; S, orthorhombic sulfur.

Table 1. Main Products Detected by XRD Characterization after the Reaction of Pure Ferrihydrite, Fh-XG and Fh-EPS Coprecipitation, with a Range of DS(-II) Concentrations for 40 Days at pH 6.0 and pH 7.5, Respectively[a]

	pH 6.0			pH 7.5		
C/Fe	S/Fe = 0.1	S/Fe = 0.5	S/Fe = 1.0	S/Fe = 0.1	S/Fe = 0.5	S/Fe = 1.0
0.0	Gt	Gt	Gt, Py	Gt	Gt, Lp	Fh
XG-0.29	Gt	Gt, S	Gt, Mk	Gt	Gt, Lp	Fh
XG-0.61	Gt	Gt	Gt, Mk	Gt	Gt	Fh
XG-1.05	Gt	Gt	Gt	Gt	Gt, Lp	Fh
XG-1.69	Gt, Lp	Gt, S	Gt, S	Gt, Lp	Gt, Lp	Fh, S
EPS-0.29	Lp	Lp	Mk, S	Lp, Gt	Lp	Mk, S
EPS-0.59	Lp	Fh, S	Mk, S	Lp, Gt	Fh	Mk, S
EPS-1.05	Fh	Fh	Mk, S	Gt	Fh	Mk
	pH 6.0 S/Fe = 0.1			pH 7.5 S/Fe = 0.1		
C/Fe	Fh-AA	Fh-PGA	Fh-XG	Fh-AA	Fh-PGA	Fh-XG
0.0	Lp, Gt	Lp, Gt	Lp, Gt	Lp	Lp	Lp
0.1	Lp, Gt	Gt	Gt	Lp	Lp, Gt	Gt
0.2	Lp, Gt	Gt	Gt	Lp, Gt	Lp, Gt	Gt
0.3	Lp	Lp, Gt	Gt	Lp	Lp, Gt	Gt
0.4	Lp	Lp	Gt	Lp	Lp, Gt	Gt, Lp
0.5	Lp	Lp	Gt	Lp	Lp, Gt	Gt, Lp
0.6	Lp	Lp	Gt	Lp	Lp, Gt	Gt, Lp

[a]Abbreviations: XG: ferrihydrite-xanthan gum coprecipitate, EPS: ferrihydrite–EPS coprecipitate; e.g., XG-0.29 means ferrihydrite-xanthan gum coprecipitate with a C/Fe molar ratio of 0.29. Fh-AA: ferrihydrite-alginic acid coprecipitate, Fh-PGA: ferrihydrite-polygalacturonic acid coprecipitate, Fh-XG: ferrihydrite-xanthan gum coprecipitate, Gt = goethite, Lp = lepidocrocite, Mk = mackinawite, Py = pyrite, S = orthorhombic sulfur.

Figure 3. (a) X-ray powder diffractograms of the Fh-AA, Fh-PGA, and Fh-XG coprecipitations with the initial C/Fe molar ratio range from 0 to 0.6 after 10 days of aging following the addition of S(-II) at S(-II)/Fe molar ratios of 0.1 at pH values 6 and 7.5. Abbreviations: G, goethite; L, lepidocrocite. (b) Photos of serum bottles corresponding to Fh−OM coprecipitations unreacted with DS(-II) and reacted with DS(-II) for 10 days were taken after 180 and 4800 s of sedimentation following vigorous mixing and resuspension, respectively. The solid−liquid interface of the mixture is marked with a green line. Full photos of the samples before and after sulfidation are shown in Figures S19 and S20.

HCl Extractable Fe. The speciation of Fe in Fh-XG coprecipitation was quantified by the stepwise extraction of the solid phase with different concentrations of HCl. The proportion of Fe(II) to total Fe (abbreviated as Fe(II) fraction) in each sample is shown in Figure S13. For all total Fe extraction treatments, there was no significant difference in the Fe(II) fraction between samples at 1 day and 40 days of intervals, indicating that the redox reactions of solid-phase Fe occurred rapidly during sulfidation (Figure S13b,d). For 0.5 M HCl extractable Fe, the Fe(II) fraction negatively correlates with the C/Fe molar ratio, while positively correlates with the S(-II)/Fe molar ratio after 1 day of aging but negatively correlates after 40 days of aging. The molar ratio of the difference between 6 M HCl extractable Fe and 0.5 M HCl extractable Fe(III) to the total solid-phase Fe is shown in Figure 1. In all treatment groups, the proportion of Fe(III)-oxides increased by 7−89% in the 40 day samples compared with that in the 1 day samples (Figures S14 and S15). The crystalline Fe(III)-oxide phase first increased and then decreased with the increasing C/Fe molar ratio, while the crystalline Fe−S phase negatively correlated with the C/Fe molar ratio.

XRD Characterization. The XRD patterns of Fh-XG and Fh-EPS coprecipitated with different C and S loadings during sulfidation demonstrated extensive mineralogical transformations (Figures 2, and S17, and S18). For Fh-XG coprecipitation, the main product in the early stage of

sulfidation was lepidocrocite under the low sulfide condition (Table 1). With the anoxic aging of the samples, lepidocrocite gradually transformed into goethite. After the addition of DS(-II), the recrystallization to Fe(III)-oxides was promoted and then inhibited with the increasing C/Fe molar ratio. The concentration of dissolved Fe(II) showed a similar trend. When the C/Fe molar ratio of coprecipitation is 0.61, the production of goethite and dissolved Fe(II) reached the maximum value. The Fh-XG coprecipitation with a C/Fe molar ratio of 1.69 still had a large amount of lepidocrocite phase after 40 days of aging.

PGA derived from plants, AA derived from algae, and XG derived from microorganisms were used to synthesize Fh−OM coprecipitation with an initial C/Fe molar ratio of 0−0.6 for anoxic aging under low sulfide conditions. Interestingly, the transformation of Fh−OM coprecipitates synthesized by all EPS proxies to crystalline Fe(III)-oxides was first promoted and then inhibited as the C/Fe molar ratio increased (Figure 3a). In addition, before reacting with DS(-II), the apparent volume of the suspension floc after a certain period of sedimentation first increased and then decreased as the OM loading increased. This phenomenon was especially obvious for the Fh-XG coprecipitation (Figure 3b). Compared with the XRD patterns, the samples containing more lepidocrocite components were more difficult to settle. In contrast, the samples whose main transformation product is goethite were almost completely settled (Figure S20).

The recrystallization of Fe(III)-oxides in the Fh-XG coprecipitation decreased under a high sulfide condition. For the pure ferrihydrite control group, XRD peaks attributed to pyrite were observed at 40 days in the high sulfide treatment group at pH 6 (Figure 2). Although the XRD peaks attributed to Fe−S minerals in XG loading groups at different time intervals were not prominent, the solid-phase HCl extractable Fe indirectly indicates the formation of Fe−S minerals (Figures 1 and S15). Mineralogical transformation of the high C/Fe molar ratio groups occurred more rapidly at pH 6 than at pH 7.5. Under the medium sulfide condition, the main product of ferrihydrite sulfidation is goethite at pH 6 and lepidocrocite at pH 7.5. Furthermore, under the high sulfide condition, the transformation of ferrihydrite to goethite at pH 6 was inhibited compared with low sulfide treatment, while no obvious XRD peak was observed at pH 7.5 (Table 1).

The XRD patterns of the Fh-EPS treatment group showed a similar mineralogical transformation. Compared with EPS proxies, microbiogenic EPS has a more apparent inhibitory effect on the mineral transformation of ferrihydrite. For all sulfide-added treatment groups, when the C/Fe molar ratio was higher than 0.59, no obvious XRD peaks were observed at either pH 6 or 7.5, even after anoxic aging for 40 days. XRD peaks attributed to mackinawite were observed in the EPS loading group but not in the XG group (Figure 2 and Table 1). A plausible explanation is that EPS has a strong inhibition on the recrystallization of Fe(III)-oxides, so the smoother XRD peaks attributed to mackinawite were revealed, while in the XG loading group, these peaks may be masked by the sharper crystalline Fe(III)-oxide peaks.

Iron K-edge XAS Characterization. Iron K-edge XAS was applied to quantitatively analyze the mineral phase of Fh-XG coprecipitation under medium and high sulfide conditions. The Fe K-edge XANES spectra (Figure S21) showed a slight shoulder near 7120 eV and shifts in the pre-edge feature toward lower energy, indicating the presence of solid-phase Fe(II), which was consistent with the result of HCl extractable Fe. The Fe K-edge EXAFS data (Figure 4) enabled the quantitative analysis of Fe transformations by LCF. They were generally consistent with the XRD results for forming Fe-bearing minerals. For the 10 day samples, the LCF fitting results indicated that about 45−56% of ferrihydrite was transformed to goethite at pH 6, while only 31−39% of goethite was formed with a small amount of lepidocrocite (6−13%) at pH 7.5. The Fe K-edge EXAFS data of the 40 day samples showed the apparent formation of Fe(III)-oxides and Fe−S secondary minerals. Comparing pure ferrihydrite with the Fh-XG coprecipitates with a C/Fe molar ratio of 0.61, the addition of XG inhibited the formation of goethite and mackinawite under the condition of high DS(-II) concentration. The production of goethite was reduced by 9.4−11.4%, and the production of mackinawite by 100% at pH 6. Ferrihydrite did not recrystallize to the Fe(III)-oxide phase except for a small amount of mackinawite formed (1−17%) under the high sulfide condition at pH 7.5, which was identified in XAS but not XRD results.

■ DISCUSSION

Mineral Transformation of Fh−OM Driven by DS(-II). Previous studies have documented that the reduction of DS(-II)-driven Fe(III)-(hydr)oxide−OM coprecipitates and mineralogical transformation in anoxic environments depend on hydrochemical conditions such as pH and DS(-II)/Fe molar
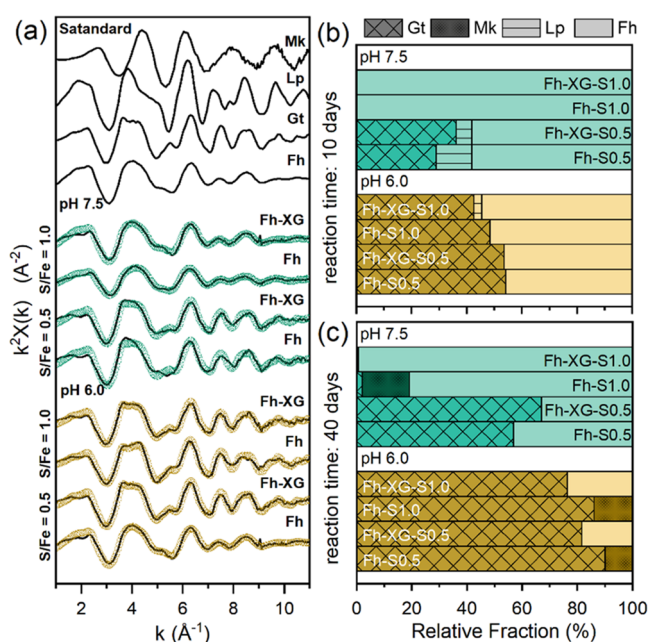
Figure 4. (a) Iron K-edge EXAFS spectra of references and LCFs of 40 days aged Fh-XG coprecipitates. Experimental data and model fits are shown as solid and dotted lines. Results from linear combination fit analyses of k^3-weighted EXAFS spectra of both 10 days (b) and 40 days (c) pure ferrihydrite and Fh-XG with a C/Fe ratio of 0.61 reacted with DS(-II) at S(-II)/Fe molar ratios of 0.5 and 1.0 at pH 6 (yellow) and 7.5 (green), respectively. Additional spectra and corresponding fit for the 10 day samples are found in Figure S18. Abbreviations: Mk, mackinawite; Lp, lepidocrocite; Gt, goethite; Fh, ferrihydrite.

ratio.[33] The reduction of the Fe(III) phase by DS(-II) is highly pH-dependent and reaches a maximum at about pH 6, which is attributed to the formation of the inner-sphere complex of S(-II) on the surface of ferrihydrite.[17,18] Therefore, the consumption rate of DS(-II) in the pH 6 treatment groups in this study was slightly higher than that in the pH 7.5 treatment groups (Figure S5).[33] If exogenous DS(-II) is added to the system within a short period, the above redox reaction is estimated to occur within 24 h, which can be proved by an insignificant difference; the proportion of Fe(II) in the total Fe was observed between the samples at time intervals of 1 day and 40 days (Figure S13). In naturally occurring sulfate-reducing conditions, the DS(-II) supply is often continuous, so the Fe(III) reduction and mineral transformation may be more complicated and involve multiple parallel pathways.[9]

Fe(II) produced by Fe(III) reduction is either released into the aqueous phase as free ferrous ions, bound to the solid phase by adsorption, or precipitated as Fe(II)-containing phase, such as by combining with excess DS(-II) to precipitate as mackinawite or as Fe(II)-hydroxide at high pH. Previous studies have widely reported that Fe(II) as catalysts can accelerate the crystallization of ferrihydrite into lepidocrocite, goethite, and magnetite in the absence of dissolved oxygen.[23,31,37,43] The process is due to the adsorption of ferrous ions on the mineral surface to promote the reductive dissolution of ferrihydrite, and the local instability caused by electron conduction leads to the Fe(III) precipitates as lepidocrocite or goethite.[23,60−62] The type of secondary Fe(III)-oxide formation is generally considered to depend on the partitioning of Fe(II) between the aqueous and solid

phases and the adsorption of Fe(II) in the solid phase.[60] Briefly, at lower pH, ferrihydrite transforms to lepidocrocite at relatively low solid-associated Fe(II) concentrations and transforms to goethite at higher solid-associated Fe(II) concentrations.[6,17] The measured solid-associated Fe(II) is determined by the extent of Fe(III) reduction and the Fe(II) partitioning, and both pathways are impacted by the coexisting OM. Therefore, Fh−OM coprecipitates exhibited a different mineralogical transformation trend compared to pure ferrihydrite (Figure 2). At higher DS(-II) concentrations (S(-II)/Fe molar ratio >0.5), the reduced Fe(II) rapidly reacted with the excess DS(-II) to form nanocrystalline mackinawite and Fe−S clusters (rapid darkening of the sample; Figure S2).[4,6,11] However, due to the poor crystallinity of the formed mackinawite, this fraction could not be detected by XRD. However, the decrease of 0.5 M HCl extractable Fe(II) phase (Figure S13) and the increase of sulfidized Fe(II) (Figure 1) at 40 days compared with those at 1 day, as well as the gradual precipitation of suspended black particles after 40 days of reaction (Figure S2), can all indirectly prove the formation of Fe−S minerals. Stoichiometrically, the S(-II)/Fe molar ratio of 1 is sufficient to oxidize DS(-II) to form mackinawite completely. However, the solid phase of the medium and high sulfide treatment groups contained a high proportion of Fe(III) phase, which was attributed to the passivation of the ferrihydrite surface by Fe(II) (adsorbed species and secondary precipitates). In addition, the OM covering the mineral surface also hinders the contact between DS(-II) and Fe(III), thereby inhibiting the formation of mackinawite (Figure 4). Compared to metastable mackinawite, pyrite forms slowly in the presence of elemental S[0] or polysulfides.[1,2,4,15,16] Previous studies have shown that the kinetics of pyrite formation is slower at high pH. Therefore, we only observed pyrite formation in the pure ferrihydrite treatment group under high sulfide conditions at pH 6 (Figure 2). The addition of OM inhibited the pyritization of ferrihydrite, which is consistent with previous reports.[33]

Effect of C/Fe Molar Ratio on Fh−OM Sulfidation. Organic matter represented by EPS can coprecipitate with ferrihydrite and affect its mineral transformation.[39,63] Previous studies have shown that the loading of OM can promote or inhibit the reductive dissolution of ferrihydrite and thus influence the formation of crystalline Fe(III)-oxides. The main influencing factors include the coupling mechanism of OM and minerals, the C/Fe molar ratio, the chemical composition of OM, and the structural disorder of the Fh−OM coprecipitate.[40,41,64] The mineral transformation of Fh-EPS and Fh-XG coprecipitates during sulfidation showed a similar trend depending on the C/Fe molar ratio (Figure 2). Unlike what has been reported in the previous work, the effect of the C/Fe molar ratio on mineral transformation is not monotonic.[31,35,65] The effect of the C/Fe molar ratio on the reductive dissolution and recrystallization of ferrihydrite exhibits a dual effect (Figures 2 and 3). The addition of OM inhibits the mineral transformation of ferrihydrite only when the C/Fe molar ratio of the Fh−OM coprecipitate exceeds the threshold.

At low S(-II)/Fe molar ratios, the dual effect of the C/Fe molar ratio on the mineral transformation of ferrihydrite to crystalline Fe(III)-oxides is mainly attributed to the addition of the negatively charged OM reducing the positive charge on the surface of the Fh−OM coprecipitates at low C/Fe molar ratios.[48] Low amounts of OM altered the surface morphology of Fh−OM coprecipitates greatly, which resulted in higher concentrations of surface-associated Fe(II) and therefore

induced the formation of goethite.[65] In addition, the increased structural disorder of ferrihydrite, which increased mineral reactivity caused by coprecipitation with low concentrations of OM, also promotes reductive dissolution. Regarding macroscopic phenomena, Fh−OM coprecipitation with a low C/Fe molar ratio showed a lower sedimentation speed, indicating smaller mineral particle sizes, which is most evident for Fh-XG coprecipitation (Figure 3b). The microscopic images also indicate that the Fh-XG coprecipitates with low C/Fe molar ratios have a more disordered microstructure than pure ferrihydrite (Figure S3). Moreover, according to classical nucleation theory, the type of secondary phase form is controlled by a delicate balance between the thermodynamic phase transition driving force and interfacial free energy.[66] Addition of OM may increase the nucleation barrier and thus inhibit the growth of lepidocrocite crystals, thus promoting the transformation to goethite (Figures 2 and 3a).[67] At high C/Fe molar ratio, OM introduced an excessive negative charge to the Fh−OM coprecipitation, which hinders the directional aggregation of mineral particles and the crystallization of secondary minerals. This is consistent with the positive correlation between the apparent precipitation volume of coprecipitation and the C/Fe molar ratio observed macroscopically (Figure S2). In addition, the encapsulation effect of OM reduces the effective reaction sites and Fe(II) accessibility on the mineral surface, thereby inhibiting the recrystallization of Fe(III)-oxides.[27,31,61] In addition, the difference in solid-associated Fe(II) caused by the addition of OM also led to differences in recrystallization to lepidocrocite or goethite (Figure 3a).

At high S(-II)/Fe molar ratios, the coprecipitation of OM with minerals inhibited the transformation of ferrihydrite to both Fe(III)-oxides and Fe−S minerals. Unlike the transformation of ferrihydrite to crystalline Fe(III)-oxides, the addition of low concentrations of OM did not promote the formation of Fe−S minerals, which may be attributed to possible different heterogeneous nucleation mechanisms of iron oxides and Fe−S phase on the surface of Fh−OM coprecipitates.[4] The addition of OM may increase the nucleation barrier and reduce the nucleation and stability of the Fe−S phase.[68] Ferrous ions are catalysts for transforming ferrihydrite into crystalline Fe(III)-oxides and precursors for forming Fe−S secondary minerals. The addition of OM inhibits the reduction of Fe(III) through surface passivation and pore blocking, thereby reducing the amount of released ferrous ions. Similar to the effect of OM on the recrystallization of Fe(III)-oxides, the addition of OM with excess negative charge changes the surface charge of the Fh−OM coprecipitates, thereby hindering the crystallization of both Fe(III)-oxides and Fe−S secondary minerals. The addition of OM prolonged the time of formation and the quantity of precursor compounds for mackinawite and pyrite formations such as aqueous Fe−S colloids or surface-bound polysulfides.[4] In addition, adding OM reduces the surface sites (SS) of ferrihydrite, thereby decreasing the reactivity of ferrihydrite while increasing the S(-II)/SS ratio. Hence, the conversion into pyrite would be suppressed if the reactivity of the ferrihydrite toward sulfide is low. This may explain why no pyrite formation was observed in Fh−OM for 40 days of aging. Furthermore, OM is capable of oxidizing DS(-II) at a rate comparable to that of DS(-II) reacting with Fe(III)-oxides in anoxic environments. OM competes with ferrous ions for sulfide, further inhibiting Fe−S secondary mineral formation.

Overall, the effect of the C/Fe molar ratio on the Fh−OM coprecipitate sulfidation depends on the amount of loaded sulfide. At low S(-II)/Fe molar ratios, DS(-II) triggers the generation of aqueous Fe(II) through electron transfer from DS(-II) to Fe(III)-oxide phases. The effect of C/Fe molar ratio on Fe(II)-induced transformation of ferrihydrite exhibits a dual effect. At high S(-II)/Fe molar ratios, Fe−S interaction dominates ferrihydrite sulfidation. The addition of OM inhibited the formation of mackinawite and pyrite.

Impact of OM Type on Fh−OM Sulfidation. Besides the C/Fe molar ratio, the chemical composition of OM is also an essential factor affecting the sulfidation of Fh−OM coprecipitates. It has been reported that the pyritization of ferrihydrite may be affected by the molecular weight of the loaded OM. The Fe−S mineralization pathway differed when Fh coprecipitated with OM having small or large molecular weight, with pyrite and greigite being the main products, respectively. Since the aging time of the samples in this study was only 40 days, pyrite formation was only detected in the pure ferrihydrite treatment group (Figure 3a). For the natural organic matter (NOM) with complex compositions, the differential molecular fractionation caused by the adsorption and coprecipitation may lead to either promotion or inhibition of the ferrihydrite transformation.[37,54,69] The coprecipitates synthesized by macromolecular polysaccharides from various sources selected in this study showed different mineral transformation pathways. Briefly, the primary product of the recrystallization of Fe(III)-oxides changed from lepidocrocite to goethite with the coprecipitate-loaded OM changing from algae to plant to microorganism-sourced EPS proxies, which indicates that the inhibitory effect of macromolecular polysaccharides on the mineral transformation of Fh−OM sulfidation is algal source > plant source > microbial source (Figure 3a), which is consistent with the carboxyl richness of these three polysaccharides. The increasing carboxyl richness of the polysaccharide leads to an increase in the number of Fe-carboxylate bonds between ferrihydrite and OM, thereby increasing the binding strength of OM and thus inhibiting the mineralogical transformation of ferrihydrite.[35] Bacteriogenic EPS is more bulky and may block more surface sites for adsorption or Fe release and thus have a stronger inhibitory effect on mineral transformation compared with microbiogenic polysaccharide (XG) under the same C/Fe molar ratio (Figure 2). Since bacteriogenic EPS is heterogeneous and contains phospholipids, proteins, fatty acids, and other components in addition to polysaccharides, the superior inhibition of ferrihydrite sulfidation by microbiogenic EPS compared with that of XG may be caused by these unaccounted components, which requires further research in the future.

Environmental Implications. Considering the ubiquitous presence of mineral−organic complexes in the natural system, our understanding of ferrihydrite sulfidation involving pure iron mineral phases under anoxic conditions may be incomplete. This study systematically explored the effect of EPS on the sulfidation of ferrihydrite. The results demonstrate that the effect of OM on the sulfidation pathway is diverse and depends on the S(-II)/Fe molar ratio as well as the coprecipitated C/Fe molar ratio and the chemical structure of the organic ligands it contains. Thus, in mineral subsoils or mining-derived mineral matrices with low S(-II)/Fe molar ratios, low concentrations of OM promote the transformation pathway of ferrihydrite sulfidation to crystalline Fe(III)-oxides. Even short-term redox fluctuations may thus alter the adsorption capacity of mineral phases and significantly affect the biogeochemical cycles of the associated pollutants and nutrients. In contrast, in organic-rich surface soils, wetlands, and marine sediments with higher S(-II)/Fe molar ratios, OM significantly inhibits ferrihydrite sulfidation, so prolonged exposure of ferrihydrite−organic coprecipitates to DS(-II) may have a limited effect on the crystallinity and transformation of the mineral phase. Sulfate reduction-induced Fh−OM coprecipitate mineral transformation may affect the mobility of nutrients and trace metals,[8,9] promoting the release of organics or their synchronous sequestration with trace metals.[14,69] Furthermore, in the current study, simple organic ligands were selected as EPS proxies, which were not expected to interact directly or significantly with DS(-II).[15,70,71] However, native EPS is heterogeneous and has a more complex composition capable of oxidizing and binding DS(-II) at a rate comparable to that of DS(-II) reacting with Fe(III)-(hydr)oxide in anoxic environments. Our results suggest that microbiogenic EPS has a more potent inhibitory effect on mineral transformation than EPS proxies. Under redox fluctuations, S(-II) binds to various components in EPS and affects its selective retention in minerals. Collectively, our results imply that EPS plays a crucial role in the formation and transformation of Fh−OM coprecipitates and Fe−C−S cycling in anoxic soils and sediments. Given the important role of Fe(III)-oxide−OM associations in the biogeochemical cycling of nutrients and trace elements, further studies need to appreciate the diversity and biogeochemical transformation of OM in redox-fluctuating environments.

■ ASSOCIATED CONTENT

ⓈI Supporting Information

The Supporting Information is available free of charge at https://pubs.acs.org/doi/10.1021/acs.est.2c06921.

> XAS characterization; elemental composition of organic ligands used in coprecipitate synthesis; experimental conditions for the Fh−OM coprecipitation sulfurization experiment; elemental composition of Fh−OM coprecipitation; flowchart of this study; sample photographs and SEM images; Fe and sulfur species data; XRD patterns; and Fe K-edge XANES spectra (PDF)

■ AUTHOR INFORMATION

Corresponding Authors

Jiajia Wang − *Department of Environmental Science and Engineering, Fudan University, Shanghai 200433, China;* ⓞ orcid.org/0000-0002-5860-5016; Email: jiajia_wang@fudan.edu.cn

Zimeng Wang − *Department of Environmental Science and Engineering, Fudan University, Shanghai 200433, China; Shanghai Institute of Pollution Control and Ecological Security, Shanghai 200433, China; National Observations and Research Station for Wetland Ecosystems of the Yangtze Estuary, Shanghai 200433, China;* ⓞ orcid.org/0000-0002-4572-629X; Email: zimengw@fudan.edu.cn

Authors

Qihuang Wang − *Department of Environmental Science and Engineering, Fudan University, Shanghai 200433, China;* ⓞ orcid.org/0000-0002-0226-2165

Xingxing Wang − *Department of Environmental Science and Engineering, Fudan University, Shanghai 200433, China;* orcid.org/0000-0001-5030-3817

Naresh Kumar − *Soil Chemistry and Chemical Soil Quality, Wageningen University and Research, Wageningen 6708, The Netherlands;* orcid.org/0000-0002-8593-5758

Zezhen Pan − *Department of Environmental Science and Engineering, Fudan University, Shanghai 200433, China;* orcid.org/0000-0003-1712-3149

Stefan Peiffer − *Department of Hydrology, University of Bayreuth, Bayreuth 95440, Germany;* orcid.org/0000-0002-8326-0240

Complete contact information is available at:
https://pubs.acs.org/10.1021/acs.est.2c06921

Notes
The authors declare no competing financial interest.

REFERENCES

(1) Peiffer, S.; Behrends, T.; Hellige, K.; Larese-Casanova, P.; Wan, M.; Pollok, K. Pyrite formation and mineral transformation pathways upon sulfidation of ferric hydroxides depend on mineral type and sulfide concentration. *Chem. Geol.* **2015**, *400*, 44−55.

(2) Wan, M.; Schröder, C.; Peiffer, S. Fe (III): S (-II) concentration ratio controls the pathway and the kinetics of pyrite formation during sulfidation of ferric hydroxides. *Geochim. Cosmochim. Acta* **2017**, *217*, 334−348.

(3) Saalfield, S. L.; Bostick, B. C. Changes in iron, sulfur, and arsenic speciation associated with bacterial sulfate reduction in ferrihydrite-rich systems. *Environ. Sci. Technol.* **2009**, *43*, 8787−8793.

(4) Wan, M.; Shchukarev, A.; Lohmayer, R.; Planer-Friedrich, B.; Peiffer, S. Occurrence of surface polysulfides during the interaction between ferric (hydr) oxides and aqueous sulfide. *Environ. Sci. Technol.* **2014**, *48*, 5076−5084.

(5) Kumar, N.; Pacheco, J. L.; Noël, V.; Dublet, G.; Brown, G. E. Sulfidation mechanisms of Fe (III)-(oxyhydr) oxide nanoparticles: a spectroscopic study. *Environ. Sci.: Nano* **2018**, *5*, 1012−1026.

(6) ThomasArrigo, L. K.; Mikutta, C.; Lohmayer, R.; Planer-Friedrich, B.; Kretzschmar, R. Sulfidization of organic freshwater flocs from a minerotrophic peatland: speciation changes of iron, sulfur, and arsenic. *Environ. Sci. Technol.* **2016**, *50*, 3607−3616.

(7) Wang, X.; Li, W.; Harrington, R.; Liu, F.; Parise, J. B.; Feng, X.; Sparks, D. L. Effect of ferrihydrite crystallite size on phosphate adsorption reactivity. *Environ. Sci. Technol.* **2013**, *47*, 10322−10331.

(8) Schoepfer, V. A.; Lindsay, M. B. Repartitioning of co-precipitated Mo (VI) during Fe (II) and S (-II) driven ferrihydrite transformation. *Chem. Geol.* **2022**, *610*, No. 121075.

(9) Burton, E. D.; Johnston, S. G.; Bush, R. T. Microbial sulfidogenesis in ferrihydrite-rich environments: Effects on iron mineralogy and arsenic mobility. *Geochim. Cosmochim. Acta* **2011**, *75*, 3072−3087.

(10) Townsend, L. T.; Shaw, S.; Ofili, N. E.; Kaltsoyannis, N.; Walton, A. S.; Mosselmans, J. F. W.; Neill, T. S.; Lloyd, J. R.; Heath, S.; Hibberd, R. Formation of a U (VI)−persulfide complex during environmentally relevant sulfidation of iron (oxyhydr) oxides. *Environ. Sci. Technol.* **2019**, *54*, 129−136.

(11) Hockmann, K.; Planer-Friedrich, B.; Johnston, S. G.; Peiffer, S.; Burton, E. D. Antimony mobility in sulfidic systems: Coupling with sulfide-induced iron oxide transformations. *Geochim. Cosmochim. Acta* **2020**, *282*, 276−296.

(12) Kumar, N.; Noël, V.; Besold, J.; Planer-Friedrich, B.; Boye, K.; Fendorf, S.; Brown, G. E., Jr Mechanism of Arsenic Partitioning During Sulfidation of As-Sorbed Ferrihydrite Nanoparticles. *ACS Earth Space Chem.* **2022**, *6*, 1666−1673.

(13) Stolze, L.; Zhang, D.; Guo, H.; Rolle, M. Model-based interpretation of groundwater arsenic mobility during in situ reductive transformation of ferrihydrite. *Environ. Sci. Technol.* **2019**, *53*, 6845−6854.

(14) Hu, S.; Zhen, L.; Liu, S.; Liu, C.; Shi, Z.; Li, F.; Liu, T. Synchronous sequestration of cadmium and fulvic acid by secondary minerals from Fe (II)-catalyzed ferrihydrite transformation. *Geochim. Cosmochim. Acta* **2022**, *334*, 83−98.

(15) Yu, Z.-G.; Peiffer, S.; Göttlicher, J.; Knorr, K.-H. Electron transfer budgets and kinetics of abiotic oxidation and incorporation of aqueous sulfide by dissolved organic matter. *Environ. Sci. Technol.* **2015**, *49*, 5441−5449.

(16) Hellige, K.; Pollok, K.; Larese-Casanova, P.; Behrends, T.; Peiffer, S. Pathways of ferrous iron mineral formation upon sulfidation of lepidocrocite surfaces. *Geochim. Cosmochim. Acta* **2012**, *81*, 69−81.

(17) Poulton, S. W. Sulfide oxidation and iron dissolution kinetics during the reaction of dissolved sulfide with ferrihydrite. *Chem. Geol.* **2003**, *202*, 79−94.

(18) Peiffer, S.; Dos Santos Afonso, M.; Wehrli, B.; Gaechter, R. Kinetics and mechanism of the reaction of hydrogen sulfide with lepidocrocite. *Environ. Sci. Technol.* **1992**, *26*, 2408−2413.

(19) Rickard, D. T. Kinetics and mechanism of pyrite formation at low temperatures. *Am. J. Sci.* **1975**, *275*, 636−652.

(20) Rickard, D. *Sulfidic Sediments and Sedimentary Rocks*; Newnes, 2012.

(21) Dos Santos Afonso, M.; Stumm, W. Reductive dissolution of iron (III)(hydr) oxides by hydrogen sulfide. *Langmuir* **1992**, *8*, 1671−1675.

(22) Hansel, C. M.; Benner, S. G.; Fendorf, S. Competing Fe (II)-induced mineralization pathways of ferrihydrite. *Environ. Sci. Technol.* **2005**, *39*, 7147−7153.

(23) Liu, H.; Li, P.; Zhu, M.; Wei, Y.; Sun, Y. Fe (II)-induced transformation from ferrihydrite to lepidocrocite and goethite. *J. Solid State Chem.* **2007**, *180*, 2121−2128.

(24) Kallenbach, C. M.; Frey, S. D.; Grandy, A. S. Direct evidence for microbial-derived soil organic matter formation and its ecophysiological controls. *Nat. Commun.* **2016**, *7*, No. 13630.

(25) Chan, C. S.; De Stasio, G.; Welch, S. A.; Girasole, M.; Frazer, B. H.; Nesterova, M. V.; Fakra, S.; Banfield, J. F. Microbial polysaccharides template assembly of nanocrystal fibers. *Science* **2004**, *303*, 1656−1658.

(26) Zhu, D.; Zhang, M.; Chen, J.; Mortimer, M.; Wu, Y.; Liu, J.; Huang, Q.; Cai, P. Synergism between goethite size and extracellular polymeric substances (EPS) in the formation of mineral−mineral and organo-mineral complexes of soil microaggregates. *Geoderma* **2022**, *410*, No. 115650.

(27) Chen, C.; Dynes, J. J.; Wang, J.; Sparks, D. L. Properties of Fe-organic matter associations via coprecipitation versus adsorption. *Environ. Sci. Technol.* **2014**, *48*, 13751−13759.

(28) Kaiser, K.; Guggenberger, G. Sorptive stabilization of organic matter by microporous goethite: sorption into small pores vs. surface complexation. *Eur. J. Soil Sci.* **2007**, *58*, 45−59.

(29) Eusterhues, K.; Neidhardt, J.; Hädrich, A.; Küsel, K.; Totsche, K. U. Biodegradation of ferrihydrite-associated organic matter. *Biogeochemistry* **2014**, *119*, 45−50.

(30) Pan, C.; Jiao, Y.; Kersting, A. B.; Zavarin, M. Plutonium Redox Transformation in the Presence of Iron, Organic Matter, and Hydroxyl Radicals: Kinetics and Mechanistic Insights. *Environ. Sci. Technol.* **2021**, *55*, 1800−1810.

(31) Chen, C.; Kukkadapu, R.; Sparks, D. L. Influence of coprecipitated organic matter on Fe2+ (aq)-catalyzed transformation of ferrihydrite: implications for carbon dynamics. *Environ. Sci. Technol.* **2015**, *49*, 10927−10936.

(32) Mikutta, C. X-ray absorption spectroscopy study on the effect of hydroxybenzoic acids on the formation and structure of ferrihydrite. *Geochim. Cosmochim. Acta* **2011**, *75*, 5122−5139.

(33) ThomasArrigo, L. K.; Bouchet, S.; Kaegi, R.; Kretzschmar, R. Organic matter influences transformation products of ferrihydrite exposed to sulfide. *Environ. Sci.: Nano* **2020**, *7*, 3405−3418.

(34) ThomasArrigo, L. K.; Bouchet, S.; Kaegi, R.; Kretzschmar, R. In *Sulfidization of Ferrihydrite in the Presence of Organic Ligands*, EGU General Assembly Conference Abstracts; EGU, 2021; pp EGU21−7701.

(35) Zhao, Y.; Moore, O. W.; Xiao, K.-Q.; Curti, L.; Fariña, A. O.; Banwart, S. A.; Peacock, C. L. The role and fate of organic carbon during aging of ferrihydrite. *Geochim. Cosmochim. Acta* **2022**, *335*, 339−355.

(36) ThomasArrigo, L. K.; Kaegi, R.; Kretzschmar, R. Ferrihydrite growth and transformation in the presence of ferrous iron and model organic ligands. *Environ. Sci. Technol.* **2019**, *53*, 13636−13647.

(37) Zhou, Z.; Latta, D. E.; Noor, N.; Thompson, A.; Borch, T.; Scherer, M. M. Fe (II)-catalyzed transformation of organic matter−ferrihydrite coprecipitates: a closer look using Fe isotopes. *Environ. Sci. Technol.* **2018**, *52*, 11142−11150.

(38) Huang, W.; Hall, S. J. Elevated moisture stimulates carbon loss from mineral soils by releasing protected organic matter. *Nat. Commun.* **2017**, *8*, No. 1774.

(39) ThomasArrigo, L. K.; Notini, L.; Shuster, J.; Nydegger, T.; Vontobel, S.; Fischer, S.; Kappler, A.; Kretzschmar, R. Mineral characterization and composition of Fe-rich flocs from wetlands of Iceland: Implications for Fe, C and trace element export. *Sci. Total Environ.* **2022**, *816*, No. 151567.

(40) Han, L.; Sun, K.; Keiluweit, M.; Yang, Y.; Yang, Y.; Jin, J.; Sun, H.; Wu, F.; Xing, B. Mobilization of ferrihydrite-associated organic carbon during Fe reduction: Adsorption versus coprecipitation. *Chem. Geol.* **2019**, *503*, 61−68.

(41) Adhikari, D.; Zhao, Q.; Das, K.; Mejia, J.; Huang, R.; Wang, X.; Poulson, S. R.; Tang, Y.; Roden, E. E.; Yang, Y. Dynamics of ferrihydrite-bound organic carbon during microbial Fe reduction. *Geochim. Cosmochim. Acta* **2017**, *212*, 221−233.

(42) Song, X.; Wang, P.; Van Zwieten, L.; Bolan, N.; Wang, H.; Li, X.; Cheng, K.; Yang, Y.; Wang, M.; Liu, T.; Li, F. Towards a better understanding of the role of Fe cycling in soil for carbon stabilization and degradation. *Carbon Res.* **2022**, *1*, No. 5.

(43) Chen, C.; Sparks, D. L. Fe (II)-induced mineral transformation of ferrihydrite−organic matter adsorption and co-precipitation complexes in the absence and presence of As (III). *ACS Earth Space Chem.* **2018**, *2*, 1095−1101.

(44) Cheng, L.; Zhu, J.; Chen, G.; Zheng, X.; Oh, N. H.; Rufty, T.; de B Richter, D.; Hu, S. Atmospheric CO2 enrichment facilitates cation release from soil. *Ecol. Lett.* **2010**, *13*, 284−291.

(45) Bottrell, S. H.; Hatfield, D.; Bartlett, R.; Spence, M. J.; Bartle, K. D.; Mortimer, R. J. Concentrations, sulfur isotopic compositions and origin of organosulfur compounds in pore waters of a highly polluted raised peatland. *Org. Geochem.* **2010**, *41*, 55−62.

(46) Burton, E. D.; Bush, R. T.; Sullivan, L. A. Fractionation and extractability of sulfur, iron and trace elements in sulfidic sediments. *Chemosphere* **2006**, *64*, 1421−1428.

(47) Matos, C. R.; Berrêdo, J. F.; Machado, W.; Metzger, E.; Sanders, C. J.; Faial, K. C.; Cohen, M. C. Seasonal changes in metal and nutrient fluxes across the sediment-water interface in tropical mangrove creeks in the Amazon region. *Appl. Geochem.* **2022**, *138*, No. 105217.

(48) Mikutta, C.; Mikutta, R.; Bonneville, S.; Wagner, F.; Voegelin, A.; Christl, I.; Kretzschmar, R. Synthetic coprecipitates of exopolysaccharides and ferrihydrite. Part I: Characterization. *Geochim. Cosmochim. Acta* **2008**, *72*, 1111−1127.

(49) Mikutta, R.; Baumgärtner, A.; Schippers, A.; Haumaier, L.; Guggenberger, G. Extracellular polymeric substances from *Bacillus subtilis* associated with minerals modify the extent and rate of heavy metal sorption. *Environ. Sci. Technol.* **2012**, *46*, 3866−3873.

(50) Knee, E. M.; Gong, F.-C.; Gao, M.; Teplitski, M.; Jones, A. R.; Foxworthy, A.; Mort, A. J.; Bauer, W. D. Root mucilage from pea and its utilization by rhizosphere bacteria as a sole carbon source. *Mol. Plant-Microbe Interact.* **2001**, *14*, 775−784.

(51) Sabra, W.; Zeng, A.-P.; Deckwer, W.-D. Bacterial alginate: physiology, product quality and process aspects. *Appl. Microbiol. Biotechnol.* **2001**, *56*, 315−325.

(52) Sutherland, I. W. Structure-function relationships in microbial exopolysaccharides. *Biotechnol. Adv.* **1994**, *12*, 393−448.

(53) Omoike, A.; Chorover, J. Adsorption to goethite of extracellular polymeric substances from *Bacillus subtilis*. *Geochim. Cosmochim. Acta* **2006**, *70*, 827−838.

(54) Zhang, M.; Peacock, C. L.; Cai, P.; Xiao, K.-Q.; Qu, C.; Wu, Y.; Huang, Q. Selective retention of extracellular polymeric substances induced by adsorption to and coprecipitation with ferrihydrite. *Geochim. Cosmochim. Acta* **2021**, *299*, 15−34.

(55) Chen, Y.; Wang, M.; Zhou, X.; Fu, H.; Qu, X.; Zhu, D. Sorption fractionation of bacterial extracellular polymeric substances (EPS) on mineral surfaces and associated effects on phenanthrene sorption to EPS-mineral complexes. *Chemosphere* **2021**, *263*, No. 128264.

(56) Shu, Z.; Pan, Z.; Wang, X.; He, H.; Yan, S.; Zhu, X.; Song, W.; Wang, Z. Sunlight-Induced Interfacial Electron Transfer of Ferrihydrite under Oxic Conditions: Mineral Transformation and Redox Active Species Production. *Environ. Sci. Technol.* **2022**, *56*, 14188−14197.

(57) Yu, Q.; Kandegedara, A.; Xu, Y.; Rorabacher, D. Avoiding interferences from Good's buffers: a contiguous series of non-complexing tertiary amine buffers covering the entire range of pH 3−11. *Anal. Biochem.* **1997**, *253*, 50−56.

(58) Claff, S. R.; Sullivan, L. A.; Burton, E. D.; Bush, R. T. A sequential extraction procedure for acid sulfate soils: partitioning of iron. *Geoderma* **2010**, *155*, 224−230.

(59) Tuccillo, M. E.; Cozzarelli, I. M.; Herman, J. S. Iron reduction in the sediments of a hydrocarbon-contaminated aquifer. *Appl. Geochem.* **1999**, *14*, 655−667.

(60) Boland, D. D.; Collins, R. N.; Miller, C. J.; Glover, C. J.; Waite, T. D. Effect of solution and solid-phase conditions on the Fe (II)-accelerated transformation of ferrihydrite to lepidocrocite and goethite. *Environ. Sci. Technol.* **2014**, *48*, 5477−5485.

(61) ThomasArrigo, L. K.; Mikutta, C.; Byrne, J.; Kappler, A.; Kretzschmar, R. Iron (II)-catalyzed iron atom exchange and mineralogical changes in iron-rich organic freshwater flocs: An iron isotope tracer study. *Environ. Sci. Technol.* **2017**, *51*, 6897−6907.

(62) Notini, L.; ThomasArrigo, L. K.; Kaegi, R.; Kretzschmar, R. Coexisting Goethite Promotes Fe (II)-Catalyzed Transformation of Ferrihydrite to Goethite. *Environ. Sci. Technol.* **2022**, *56*, 12723−12733.

(63) Yan, W.; Guo, W.; Wang, L.; Jing, C. Extracellular polymeric substances from Shewanella oneidensis MR-1 biofilms mediate the transformation of Ferrihydrite. *Sci. Total Environ.* **2021**, *784*, No. 147245.

(64) Shimizu, M.; Zhou, J.; Schröder, C.; Obst, M.; Kappler, A.; Borch, T. Dissimilatory reduction and transformation of ferrihydrite-humic acid coprecipitates. *Environ. Sci. Technol.* **2013**, *47*, 13375−13384.

(65) ThomasArrigo, L. K.; Byrne, J. M.; Kappler, A.; Kretzschmar, R. Impact of organic matter on iron (II)-catalyzed mineral transformations in ferrihydrite−organic matter coprecipitates. *Environ. Sci. Technol.* **2018**, *52*, 12316−12326.

(66) Li, X.; Sheng, A.; Ding, Y.; Liu, J. A model towards understanding stabilities and crystallization pathways of iron (oxy-

hydr) oxides in redox-dynamic environments. *Geochim. Cosmochim. Acta* **2022**, *336*, 92−103.

(67) Pedersen, H. D.; Postma, D.; Jakobsen, R.; Larsen, O. Fast transformation of iron oxyhydroxides by the catalytic action of aqueous Fe (II). *Geochim. Cosmochim. Acta* **2005**, *69*, 3967−3977.

(68) Son, S.; Hyun, S. P.; Charlet, L.; Kwon, K. D. Thermodynamic stability reversal of iron sulfides at the nanoscale: Insights into the iron sulfide formation in low-temperature aqueous solution. *Geochim. Cosmochim. Acta* **2022**, *338*, 220−228.

(69) Ma, W.-W.; Zhu, M.-X.; Yang, G.-P.; Li, T.; Li, Q.-Q.; Liu, S.-H.; Li, J.-L. Stability and molecular fractionation of ferrihydrite-bound organic carbon during iron reduction by dissolved sulfide. *Chem. Geol.* **2022**, *594*, No. 120774.

(70) Heitmann, T.; Blodau, C. Oxidation and incorporation of hydrogen sulfide by dissolved organic matter. *Chem. Geol.* **2006**, *235*, 12−20.

(71) Hoffmann, M.; Mikutta, C.; Kretzschmar, R. Bisulfide reaction with natural organic matter enhances arsenite sorption: insights from X-ray absorption spectroscopy. *Environ. Sci. Technol.* **2012**, *46*, 11788−11797.